J. Fluid Mech. (2009), *vol.* 638, *pp.* 117–140.

doi:10.1017/S0022112009990826

Entrainment waves in decelerating transient turbulent jets

MARK P. B. MUSCULUS†

Sandia National Laboratories, MS 9053, PO Box 969, Livermore, CA 94551-0969, USA

(Received 25 August 2008; revised 16 June 2009; accepted 16 June 2009; first published online 1 October 2009)

A simplified one-dimensional partial differential equation for the integral axial momentum flux during the deceleration phase of single-pulsed transient incompressible jets is derived and solved analytically. The wave speed of the derived first-order nonlinear wave equation shows that the momentum flux transient from the deceleration phase propagates downstream at twice the initial jet penetration rate. Transient-jet velocity data from the existing literature is shown to be consistent with this derivation, and an algebraic analytical solution matches the measured timing and decay of axial velocity after the deceleration transient. The solution also shows that a wave of increased entrainment accompanies the deceleration transient as it travels downstream through the jet. In the long-time limit, the peak entrainment rate at the leading edge of this 'entrainment wave' approaches an asymptotic value of three times that of the initial steady jet. The rate of approach to the asymptotic behaviour is controlled by the deceleration rate, which suggests that rate-shaping may be tailored to achieve a desired mixing state at a given time after the end of a single-pulsed jet. In the wake of the entrainment wave, the absolute entrainment rate eventually decays to zero. The local injected fluid concentration also decays, however, so that entrainment rate relative to the local concentration of injected fluid remains higher than in the initial steady jet. An analysis of diesel engine fuel-jets is provided as one example of a transient-jet application in which the considerable increase in the mixing rate after the deceleration phase has important implications.

1. Introduction

While steady jets have been widely studied and are well understood, the mixing and entrainment processes of decelerating transient jets are not well understood. A few studies have shown that during the deceleration phase of single transient jets, entrainment can be increased by a factor of two or more compared to steady jets (Borée *et al.* 1997; Johari & Paduano 1997). Bremhorst & Hollis (1990) observed similar behaviour in fully modulated multi-pulsed jets. Johari & Paduano (1997) proposed that the increase in entrainment may be due to a change in the balance of source fluid for the growth of large structures in the jet flow. They speculated that

---

† Email address for correspondence: mpmuscu@sandia.gov

during a deceleration, decreasing axial flow in the jet provides less fluid for the growth of large structures, so that ambient fluid entrainment must increase to compensate. Breidenthal (1986) proposed a similar but converse mechanism for 'accelerating' jets, where entrainment decreases to compensate for increasing velocity and vorticity from the jet source. Indeed, later experiments showed that accelerating jets display less entrainment than steady jets (Kato, Groenewegen & Breidenthal 1987; Zhang & Johari 1996). Recently, Breidenthal (2008) extended this argument to a whole class of turbulent flows, for which acceleration causes dissipation and entrainment rates to decrease.

The increased entrainment in the decelerating part of the jet also propagates downstream to affect the initial steady jet. Borée *et al.* (1997) measured the spatial and temporal evolution of axial velocities after a deceleration phase and showed that the region of increased entrainment grows in axial extent as it propagates downstream. The ways that the effects of a deceleration phase evolve spatially and temporally are very important for applications of transient jets, where mixing of jet and ambient fluids significantly influence the performance of practical devices. One important example of this type of application is the fuel-injection process in diesel engines. Recent measurements have shown that diesel jets experience greater mixing rates during and after a deceleration phase (Musculus *et al.* 2007). The increased mixing is desirable because it can lead to lower soot formation by minimizing fuel-rich mixtures, but at the same time, over-mixing can lead to mixtures that are too fuel-lean to achieve complete combustion (Musculus *et al.* 2007; Genzale, Reitz & Musculus 2008). If mixing is to be optimized for various applications, understanding of the spatial and temporal evolution of the increased entrainment region after a deceleration phase is important.

In this study, using appropriate assumptions that are supported by experimental observations, a simplified partial differential equation is derived to analyse the mixing and entrainment characteristics of incompressible round turbulent single-phase jets during and after a transient deceleration. The goal of the analysis is not to simulate decelerating jets with high fidelity but rather to provide a simplified analysis that reveals the overall evolution of entrainment in decelerating jets. As will be shown, the derived nonlinear wave equation for jet axial momentum has an analytical solution, for which a wave of increased entrainment propagates downstream. The analysis shows that entrainment can increase by as much as a factor of three during and after the transient deceleration, which helps to explain the rapid mixing observed in decelerating jets. An analytical solution to the governing equation is shown to agree well with experimental data from several decelerating-jet studies. Finally, some implications for one transient-jet application, the diesel engine, are discussed.

2. Formulation of the problem

2.1. *Governing equation*

The mixing and spreading characteristics of steady incompressible turbulent single-phase jets have been well established in numerous studies in the scientific literature and in textbooks (for example Abramovich 1963; Hinze 1975; Schlichting 1979). Much information is also available for the initial penetration during the transient start-up (see Hill & Ouellette 1999; Joshi & Schreiber 2006; Sangras, Kwon & Faeth 2002 and the references cited therein). Comparatively little information is available for the deceleration phase at the end of a transient jet. In this section, a partial differential equation for the jet axial momentum during the deceleration transient is derived.

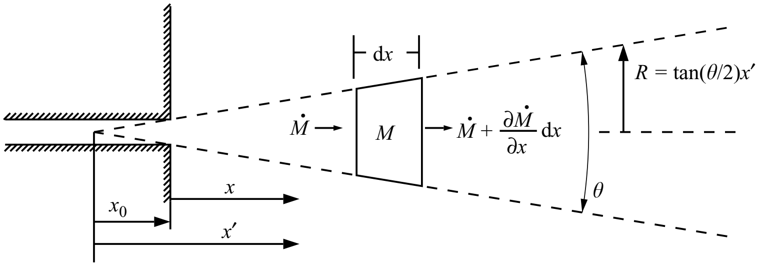

FIGURE 1. Illustration of the jet model coordinate system and integral momentum flux transport.

Consider a conical jet issuing from a round nozzle, as depicted in figure 1. The dashed lines indicate the jet boundaries, which are defined according to the axial-velocity profile, as described below. The fully developed mean axial-velocity profile is well represented by a Gaussian error curve for both single-phase (Hinze 1975; Schlichting 1979) and two-phase (Wu, Santavicca & Bracco 1984; Doudou 2005) steady jets, but Abramovich (1963) also proposed a more versatile polynomial form:

$$\frac{\bar{u}(x,\xi)}{\bar{u}_c(x)} = (1-\xi^{\alpha})^2 . \tag{2.1}$$

In (2.1), $\bar{u}_c(x)$ is the turbulent mean axial velocity on the jet centreline at downstream distance x and $\bar{u}(x,\xi)$ is the mean axial-velocity component as a function of the non-dimensional radial coordinate $\xi = r/R$, where r is the radial coordinate and R is the jet width shown in figure 1. Abramovich (1963) used $\alpha = 1.5$, for which (2.1) approximates a Gaussian error curve, to match experimentally measured velocity profiles. Later, it will be shown that the consequence of the velocity profile on the integral axial momentum of the jet can be reduced to a single coefficient, so that the exact form of the velocity profile is not critical.

The polynomial form of (2.1), rather than a Gaussian error curve, is useful because of two important features. First, (2.1) is particularly convenient for the mathematical analysis of this study because it does not have the infinite ‘wings’ of a Gaussian curve, so that the jet boundary is unambiguous. Here, the jet boundary is at $\xi = 1$, where $\bar{u}(z,\xi) = 0$. This boundary definition corresponds to the position at which the axial velocity on a Gaussian error curve fit is approximately 3 % of the centreline velocity. (A slight adjustment to the jet spreading angle can effectively account for fluid momentum in the low-velocity wings). Second, and more importantly, larger values of α produce flatter profiles that are similar to those in the developing jet, approaching a uniform ‘top-hat’ velocity profile as α approaches infinity. This profile adjustment feature of (2.1) is useful for approximating the behaviour of the jet in the developing near-nozzle region, where the radial velocity profiles are flatter than in the developed jet.

Shown in figure 2 is a comparison of the velocity profiles of (2.1) with measurements from Crow & Champagne (1971) for the developing region of a $Re_d = 10^5$ steady air jet. The abscissa scale is the radial position r in the jet normalized by the radius $r_{0.2}$, where the mean axial velocity is 20 % of its centreline value. For each downstream measurement location, the value of α in (2.1) is chosen empirically to fit the measured data. In general, with judicious choice of α, the agreement between (2.1) and measured data is reasonable, except in the wings of the jet. At large radii, (2.1) has zero velocity, whereas the measured velocity is small but non-zero. At eight diameters downstream of the nozzle ($z/D_0 = 8$), where turbulent jets typically become fully developed (Hinze 1975), a Gaussian error curve (dashed line) fits the measured data quite well, as does

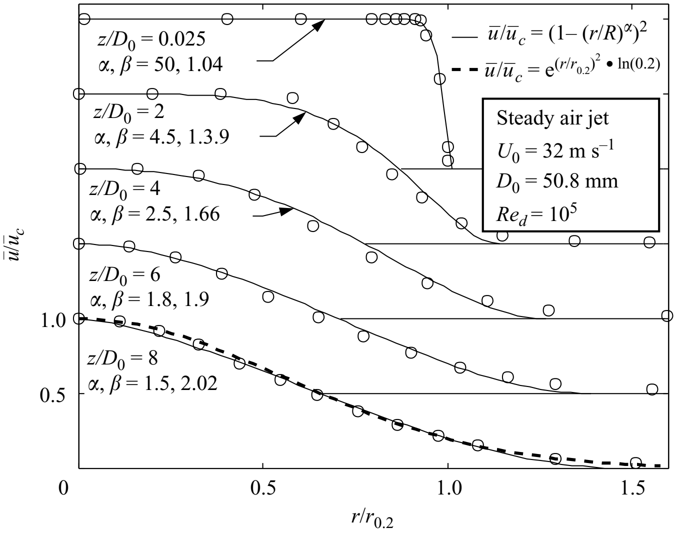

FIGURE 2. Mean axial-velocity profiles in the developing region of a $Re_d = 10^5$ steady air jet with exit velocity $U_0 = 32\,\mathrm{m\,s^{-1}}$ at the exit of a nozzle with diameter $D_0 = 50.8$ mm. Measured data (circles) are from Crow & Champagne (1971); the profiles from (2.1) (solid lines) are shown at five different downstream locations; and a Gaussian error curve (dashed line) is shown for the farthest downstream measurement location. For clarity, the data and curves for each successive measurement location are offset vertically by 0.5 $\bar{u}/\bar{u}_c$. The scale on the abscissa is the radial position r in the jet normalized by the radius $r_{0.2}$, where the mean axial velocity is 20 % of its centreline value.

(2.1), using $\alpha = 1.5$. At greater distances downstream, the profile is self-similar, so that no further adjustment from $\alpha = 1.5$ is required.

With (2.1) and the jet boundaries defined, the integral momentum M in the axial direction for a differential control volume within the jet (figure 1) is

$$M = \rho A \bar{\bar{u}}\, dx, \tag{2.2}$$

where ρ is the density and $\bar{\bar{u}}$ is the mean axial velocity averaged over the jet cross-sectional area A:

$$\bar{\bar{u}}(x) = \frac{\displaystyle\int \bar{u}\,(x,\xi)\,\mathrm{d}A}{\displaystyle\int \mathrm{d}A} = \frac{\alpha^2}{(\alpha+1)\,(\alpha+2)}\bar{u}_c(x). \tag{2.3}$$

The total axial momentum flux $\dot{M}$ integrated over the jet cross-section is

$$\dot{M} = \rho \int \bar{u}^2\,(z,\xi)\,\mathrm{d}A = \beta \pi R^2 \rho \bar{\bar{u}}^2, \tag{2.4}$$

$$\text{where } \beta = \frac{6\,(\alpha+1)\,(\alpha+2)}{(3\alpha+2)\,(2\alpha+1)}. \tag{2.5}$$

In the near-nozzle region, where α approaches infinity and the profile is uniform, (2.3) and (2.4) show that $\bar{u}_c\,(x) = \bar{\bar{u}}\,(x)$ and $\beta = 1$, consistent with a uniform or 'top-hat' exit velocity profile. For a fully developed jet with $\alpha = 1.5$, $\bar{u}_c\,(x) = \left(35/9\right)\bar{\bar{u}}\,(x)$ and $\beta = 105/52$ or approximately $\beta = 2$. Importantly, the above integral analysis leading to (2.4) shows that the effect of the velocity profile on the total momentum flux can be represented by a 'single factor' β. For any arbitrary velocity profile, therefore, the total momentum flux is simply the product of some coefficient β and the momentum flux $\pi R^2 \rho \bar{\bar{u}}^2$ calculated using the average velocity $\bar{\bar{u}}$.

Using the expression for R in figure 1, (2.4) can be rearranged for the cross-sectionally averaged velocity,

$$\bar{\bar{u}} = \sqrt{\frac{\dot{M}}{\pi \beta \rho} \frac{\cot(\theta/2)}{x'}}, \tag{2.6}$$

where θ is the full spreading angle at the edge of the jet, where $\xi = 0$. For a steady jet, the integral axial momentum flux $\dot{M}$ is constant and equal to $\dot{M}_0$ at the nozzle exit (Schlichting 1979), so that (2.6) can be written as

$$\bar{\bar{u}}_{steady} = R_0 \cot(\theta/2) \frac{\bar{\bar{u}}_0}{x' \sqrt{\beta}}, \tag{2.7}$$

where $\bar{\bar{u}}_0$ is the velocity at the nozzle exit of radius R_0. Using (2.3), (2.7) gives the familiar $1/x'$ dependence of the centreline velocity relative to the virtual origin. Note that in typical centreline velocity correlations, the virtual origin is located about three diameters downstream of the nozzle (Borée, Atassi & Charnay 1996; Reynolds *et al.* 2003) rather than behind it, as in figure 1. In such correlations, β is effectively treated as constant, so that the centreline velocity fit on $1/x'$ is improved if the origin is shifted to a downstream position at which the velocity profile approaches self-similar behaviour and β is constant. Here, however, the virtual origin defines the 'width' of the jet, rather than the centreline velocity, and β accounts for the developing velocity profile. The appropriate position for the virtual origin in this development is therefore behind the nozzle exit (figure 1). With the differential momentum and momentum flux defined in (2.2) and (2.4), a partial differential equation for the transport of momentum in the jet during the deceleration transient may be derived if the following six simplifying assumptions are applied:

(i) Density is constant throughout the jet, which implies that the jet is effectively isothermal and that the density of the injected fluid is equal to that of the ambient. For flows with different injected and ambient fluid densities, an effective nozzle diameter may be assigned according to the square root of the density ratio (Ricou & Spalding 1961; Nathan *et al.* 2006).

(ii) Turbulent (and molecular) viscous forces acting on the control volume are neglected. The normal viscous forces are typically small compared to pressure forces, and viscous shear forces at the outer radius of the jet control volume can be neglected also, since velocities and their gradients at the boundary are small.

(iii) Axial mixing of momentum due to molecular and turbulent diffusion is neglected. As a result, only axial convection of momentum in figure 1 is considered in the development of the governing equation for momentum transport. The implications of this simplification are addressed later, after the development of the momentum transport equation.

(iv) The net force due to any axial pressure gradient is assumed negligible. This is a reasonable assumption for steady jets (Hinze 1975), and the appropriateness of this assumption for decelerating jets also will be addressed later.

(v) The jet cross-sectional area remains constant during and after the deceleration phase. Several decelerating-jet experiments show that the spreading angle remains approximately constant, or even increases slightly, during the deceleration transient. Atassi, Boree & Charnay (1993) and Borée *et al.* (1996) observed that the width of the normalized mean axial-velocity profile increased by at most 15 % at the half-centreline velocity in a decelerating air jet. In diesel jets, Doudou (2005) reported similar behaviour of velocity profiles, and both Bruneaux (2005) and Musculus *et al.* (2007) observed that the scalar jet boundaries increase only gradually during and after the deceleration transient. Shadowgraph movies of non-combusting diesel jets also show that the perimeter of the jet does not markedly change during the deceleration transient, though it does gradually increase thereafter (Pickett 2009). Based on the above consistent experimental observations, as a reasonable approximation, the spreading angle during and after the deceleration transient is treated as constant at the same value as that of the steady jet. As the residual jet flow evolves and gradually widens after the end of the transient, the assumption of a constant spreading angle becomes less valid, the implications of which are examined in a later section.

(vi) The radial profile of mean axial velocity, and hence β, remains unchanged during the deceleration transient. Experimental measurements in both decelerating air jets (Atassi *et al.* 1993) and decelerating diesel jets (Doudou 2005) support this assumption, showing very similar profiles for a reasonable time after the transient. Additionally, Bremhorst (1979) reported that the velocity profiles in a variety of modulated jets, which have periodic variations in injection velocity, also remain comparable to those of a steady jet, even with large-amplitude fluctuations.

Accepting the above assumptions, a simplified integral momentum transport equation in the axial direction for the differential control volume in figure 1 may be written as

$$\frac{\partial M}{\partial t} = -\frac{\partial \dot{M}}{\partial x}\,\mathrm{d}x. \tag{2.8}$$

Using (2.2) and (2.4) and simplifying, (2.8) becomes

$$\frac{\partial}{\partial t}\left(\sqrt{\frac{\rho A \dot{M}}{\beta}}\,\mathrm{d}x\right) = -\frac{\partial \dot{M}}{\partial x}\,\mathrm{d}x.$$

Noting that $\partial\sqrt{\dot{M}}/\partial t = (\partial \dot{M}/\partial t)/(2\sqrt{\dot{M}})$ and that neither ρ and β nor A change with time (from assumptions (i), (v) and (vi)), and rearranging, yields a partial differential equation for $\dot{M}$:

$$\frac{\partial \dot{M}}{\partial t} = -2\sqrt{\frac{\beta \dot{M}}{\rho A}}\frac{\partial \dot{M}}{\partial x}. \tag{2.9}$$

Equation (2.9) is a nonlinear first-order wave equation, with local wave speed $c_{wave} = 2\sqrt{\beta \dot{M}/\rho A}$. It is also instructive to express the wave speed in (2.9) in terms of the mean velocity $\bar{\bar{u}}$, using (2.4),

$$\frac{\partial \dot{M}}{\partial t} = -2\beta\bar{\bar{u}}\frac{\partial \dot{M}}{\partial x}, \tag{2.10}$$

so that the local wave speed is $c_{wave} = 2\beta\bar{\bar{u}}$. As will be shown later, because of the lack of an axial pressure gradient (assumption (iv)), the axial velocity may be solved from the form of the momentum equation in (2.10), independent of the continuity equation. After (2.10) is solved, the continuity equation effectively provides a solution for the amount of entrainment necessary to maintain a zero axial pressure gradient and a constant spreading angle, as described in the following section.

2.2. *The entrainment wave*

Applying continuity to the differential control volume in figure 1, the entrainment rate $\partial \dot{m}_e/\partial x$ (entrained mass flux $\dot{m}_e$ per unit axial distance) is the axial derivative of the axial mass flux in the jet (Crow & Champagne 1971; Hinze 1975). The axial mass flux $\dot{m}$ is

$$\dot{m} = \rho A \bar{\bar{u}} = \sqrt{\frac{\rho A \dot{M}}{\beta}}, \tag{2.11}$$

so the entrainment rate is

$$\frac{\partial \dot{m}_e}{\partial x} = \frac{\partial \dot{m}}{\partial x} = \sqrt{\frac{\rho}{\beta}} \left(\sqrt{A} \frac{\partial \sqrt{\dot{M}}}{\partial x} + \sqrt{\dot{M}} \frac{\partial \sqrt{A}}{\partial x} \right). \tag{2.12}$$

For later analysis, it is useful to define the entrainment rate for a steady jet. In a steady jet, the momentum flux gradient $\partial \dot{M}/\partial x$ is zero, and using $A = \pi(\tan(\theta/2)x)^2$ according to the illustration in figure 1, the steady-jet entrainment rate is

$$\frac{\partial \dot{m}_{e,steady}}{\partial x} = \sqrt{\frac{\pi \rho \dot{M}_0}{\beta}} \tan\left(\frac{\theta}{2}\right), \tag{2.13}$$

where $\dot{M}_0$ is the momentum flux at the nozzle.

When a perturbation $\partial \dot{M} \big/ \partial t$ is introduced, (2.10) shows that an axial momentum flux gradient $\partial \dot{M}/\partial x$ must arise. During the deceleration transient, the $\partial \dot{M}/\partial t$ perturbation at the nozzle is negative, so (2.10) shows that the momentum flux gradient becomes locally positive. Then, according to the continuity considerations in (2.12), with positive $\partial \dot{M}/\partial x$, the entrainment rate must increase over that for a steady jet.

With a positive $\partial \dot{M}/\partial x$ in a decelerating jet, the momentum throughout the flow is affected by the passage of a wave, according to (2.10). This wave is not an acoustic wave but rather an ‘entrainment wave’, as it arises from the effects of entrainment on the momentum gradient. Momentum exchange with entrained fluid, which has negligible momentum in the axial direction, causes a reduction in the jet axial velocity in the upstream region in which entrainment is greater than in the downstream, initially steady jet. This reinforces the axial momentum flux gradient $\partial \dot{M}/\partial x$ introduced at the nozzle and propagates it downstream.

Unlike an acoustic wave, whose speed is a function of the material properties, the speed of the entrainment wave is a multiple of the flow speed, as described by (2.10). But somewhat akin to an acoustic wave, the entrainment wave is ‘faster’ than the ‘mean’ material velocity $\bar{\bar{u}}$. Indeed, the entrainment wave is also faster than the initial jet penetration rate. As described by Naber & Siebers (1996), the penetration rate of the head of the jet can be expressed as the ratio of momentum and mass fluxes. Using (2.4) and (2.11), the penetration rate of the head of the jet is

$$c_{Head} = \frac{d}{dt}(x'_{Head}) = \frac{\dot{M}}{\dot{m}} = \beta \bar{\bar{u}} = \sqrt{\frac{\beta \dot{M}}{\pi \rho} \frac{\cot(\theta/2)}{x'_{Head}}}, \tag{2.14}$$

where x'_{Head} is the downstream position of the head. Equation (2.14) may be solved for the penetration distance x'_{Head} by integration:

$$x'_{Head} = \left(\frac{\beta \dot{M}}{\pi \rho}\right)^{1/4} (2\cot(\theta/2) \cdot t)^{1/2}. \tag{2.15}$$

Using $\theta = 28^\circ$, (2.15) agrees well with established correlations for gas-jet penetration (e.g. Hill & Ouellette 1999) and entrainment (Ricou & Spalding 1961), as well with typical velocity profile widths (Hinze 1975). Comparing (2.14) with the wave speed in (2.10), we see that the propagation speed of the momentum transient is twice the

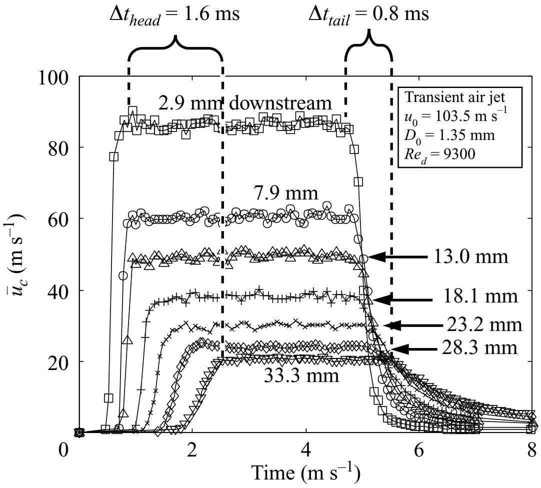

FIGURE 3. Measured ensemble-averaged centreline hot-film velocity data in a single-pulsed air jet issuing from a 1.35 mm diameter nozzle at 103.5 m s^{-1} (from Witze 1980, 1983).

initial jet penetration rate. As a result, (2.10) shows that the momentum transient of a decelerating jet will ‘catch up’ with the head of the jet at a time of about two pulse durations after the start of a single transient-jet pulse. There is only limited published experimental data to validate this derivation, but the available evidence reviewed below is consistent with (2.10) relative to (2.14).

First, Witze used hot-wire anemometry to measure centreline velocities at various axial positions in single-pulsed air jet issuing from a nozzle of diameter $D_0 = 1.35$ mm (Witze 1980, 1983). Using fast valve actuation (velocity 1/e rise time approximately 0.1 ms, fall time approximately 0.2 ms), the air jet rapidly reached a nozzle velocity of $u_0 = 103.5$ m s^{-1} and ended abruptly after about 4 ms. Figure 3 shows ensemble-averaged centreline velocities measured at several downstream positions in the transient jet. For each axial location, the velocity rises as the head of the jet arrives, remains relatively steady for several milliseconds and then falls after the end of injection. The head of the jet, marked here by the position at which the velocity reaches its steady plateau, arrives at the 2.9 mm downstream position approximately at time $t = 0.95$ ms, as indicated by the annotations in figure 3. At the 33.3 mm downstream position, the head arrives at $t = 2.55$ ms or about 1.6 ms later.

At the tail end of the jet, the edge of the entrainment wave is indicated by the departure from the steady velocity, where the momentum flux gradient becomes non-zero. As identified by the annotations in figure 3, the entrainment wave arrives at approximately $t = 4.75$ ms and $t = 5.55$ ms for the two positions, for a difference of 0.8 ms. Thus, these data show that the transit time for the entrainment wave at the tail of the jet to cross from 2.9 to 33.3 mm downstream (0.8 ms) is half that of the initial head of the jet (1.6 ms). This is consistent with the wave speed in (2.10) for the entrainment wave, which propagates downstream at twice the initial jet penetration rate of (2.14).

The decelerating air-jet data of Atassi *et al.* (1993) and Borée *et al.* (1996, 1997) support (2.10) in another way. In their jet, the exit velocity at the nozzle was initially held steady and then rapidly decelerated to half its initial value. As described in the Appendix, the temporal and spatial gradients of velocity in the middle of the transient are roughly consistent with (2.10). From continuity considerations, Borée *et al.* (1996,

1997) also inferred from their axial-velocity measurements that the entrainment velocity clearly increases during the transient, consistent with the discussion above and with (2.12) for positive $\partial \dot{M}/\partial x$.

A third example is a two-phase diesel jet injected into an atmosphere of high-molecular-weight sulphur hexafluoride, in which Doudou (2005) measured spray droplet velocities throughout the injection event. After the end of injection, the leading edge of the momentum transient, indicated by a departure of the centreline velocity from that of the initial quasi-steady jet, travelled downstream approximately twice as fast as the initial head of the jet. Furthermore, as shown in a later section, the change in penetration rate that accompanies the arrival of the entrainment wave at the head of the jet provides further evidence of the transit speed of the entrainment wave.

Thus, both (2.10) and analysis of available experimental data show that the momentum flux transient travels downstream at roughly twice the speed of the initial penetrating jet. An important consequence of this conclusion is that the increased entrainment associated with the jet deceleration not only affects the tail end of the jet in the vicinity of the deceleration but rather eventually affects the entire jet as it propagates downstream.

3. An analytical solution

3.1. *Axial velocity*

Equation (2.9) or (2.10) may be solved analytically using the method of characteristics (Kevorkian 1996; Levandosky 2008). To do so, the value of β must be treated as constant in time and space. Although β varies axially in the near-nozzle region (see figure 1 and the related discussion), it is constant in most of the downstream jet. As described in the previous section, in the downstream jet, β remains approximately constant in time throughout the deceleration transient. A solution using constant β is therefore appropriate for the entire developed portion of the jet ($x/D_0 > 8$), but it is increasingly inaccurate close to the nozzle exit when the fully developed value ($\beta = 2$) is used.

Using a constant β and expressing the jet cross-sectional area A according to the jet radius in figure 1, (2.9) may be written as

$$\frac{\partial \dot{M}}{\partial t} = -2\cot(\theta/2)\sqrt{\frac{\beta}{\rho\pi}}\frac{\sqrt{\dot{M}}}{x'}\frac{\partial \dot{M}}{\partial x}. \tag{3.1}$$

The method of characteristics analysis shows that the general solution to (3.1) is

$$\sqrt{\dot{M}(x', t)} = f(\phi), \tag{3.2}$$

where the coordinate ϕ is

$$\phi = (x')^2 - 4\cot\left(\frac{\theta}{2}\right)\sqrt{\frac{\beta}{\pi\rho}}\sqrt{\dot{M}}t. \tag{3.3}$$

While (3.2) and (3.3) comprise a valid general solution to (3.1), a more mathematically convenient solution to (3.1) uses an inverse function of (3.2):

$$\phi = g(\sqrt{\dot{M}}). \tag{3.4}$$

To solve (3.1), an appropriate function $g(\sqrt{\dot{M}})$ must be selected to satisfy the velocity boundary conditions at the nozzle exit during the deceleration transient. One candidate function is a second-order polynomial:

$$g(\sqrt{\dot{M}}) = A(\sqrt{\dot{M}})^2 + B\sqrt{\dot{M}} + C. \tag{3.5}$$

For the above function, three points during the transient are required to define A, B and C for the boundary condition at the nozzle exit, where $x' = x_0$ (figure 1). First, at the beginning of the deceleration transient ($t = 0$), the velocity at the nozzle is equal to that of the initial steady jet, which implies $\sqrt{\dot{M}} = \sqrt{\dot{M}_0}$. Second, at some time $t_{1/2}$ after the start of the transient, the velocity at the nozzle falls to one half of its initial value, or $\sqrt{\dot{M}} = \sqrt{\dot{M}_0}/2$. Third, at the end of the transient, the velocity is zero at the nozzle. Using (3.5) in (3.4) after determining A, B and C from the boundary conditions, and using (3.3), gives an analytical solution for $\sqrt{\dot{M}}$:

$$\sqrt{\dot{M}} = \sqrt{\left(\frac{t}{2t_{1/2}} - 1\right)^2 \frac{\dot{M}_0}{4} - \tan\left(\frac{\theta}{2}\right)\sqrt{\frac{\pi\rho\dot{M}_0}{\beta}}\,\frac{(x_0)^2 - (x')^2}{8t_{1/2}}} - \left(\frac{t}{2t_{1/2}} - 1\right)\frac{\sqrt{\dot{M}_0}}{2}. \tag{3.6}$$

The above solution applies within the transient region, i.e. where

$$\phi_0 = (x')^2 - 4\cot\left(\frac{\theta}{2}\right)\sqrt{\frac{\beta}{\pi\rho}}\sqrt{\dot{M}_0}t < (x_0)^2. \tag{3.7}$$

Outside the transient region, $\sqrt{\dot{M}}$ is equal to $\sqrt{\dot{M}_0}$ of the initial steady jet (which is constant for $x' > x_0$).

For Witze's (1980) experiment, the exit velocity falls to one half its initial value after approximately 0.15 ms, so $t_{1/2} = 0.15$ ms in (3.6) is appropriate for his jet. A comparison of the centreline velocity, using (2.3) and (2.4) and the solution of (3.6), with Witze's experimental data is shown in figure 4. Several features of figure 4 merit discussion.

First, for positions 13 mm and farther downstream, the axial decay of the centreline velocity of the quasi-steady jet, where the centreline velocity is relatively constant, is well captured by (2.6) with (2.1). This observation helps to validate the value of $\beta = 2$ for the velocity profile and the choice of $\theta = 28°$ for the spreading angle. For the near-nozzle positions, at 2.9 and 7.9 mm downstream, values of $\beta = 1.6$ and $\beta = 1.9$, respectively, were arbitrarily assigned to fit the steady velocity data, though these values are roughly consistent with the typical values of β in the developing region shown in figure 2.

A second important feature in figure 4 is that the timing of the arrival of the momentum transient, marked by the departure from the quasi-steady velocity, is also well captured. This feature is a consequence of the wave speed in (2.10). Third, the decay rate of the centreline velocity after the arrival of the momentum transient is described reasonably well, though the velocity solution is generally somewhat greater than the measurements, as shown more clearly in the inset of figure 4. The assumption of a constant spreading angle during the deceleration transient is likely to give a larger velocity in the analytical solution. If the jet width were 15 % larger during the transition, as the data of Atassi *et al.* (1993) indicate, then according to (2.10), the velocity would be 15 % lower for a given momentum flux in the solution. Furthermore, as described at the end of the Appendix, the slight velocity

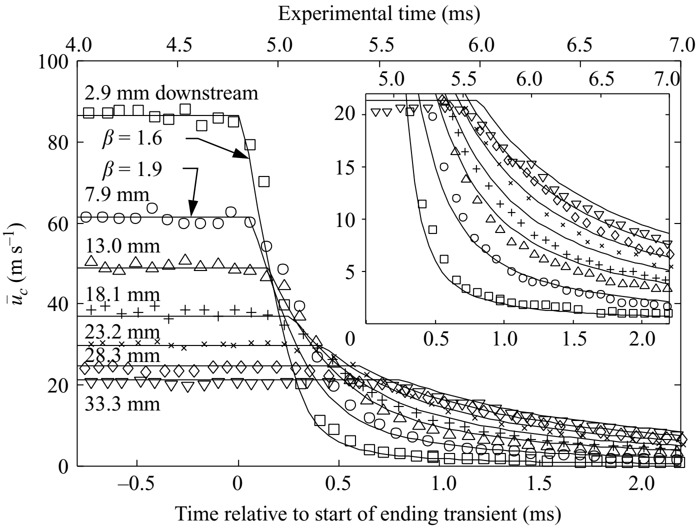

FIGURE 4. Ensemble-averaged measured data (symbols) and solution from (3.6) (solid lines) for the pulsed air jet of Witze (1980, 1983) (also see figure 2). For all solutions, $\beta = 2$ (fully developed jet) unless otherwise noted.

under-shoot observed in the decelerated jet data of Atassi *et al.* (1993) and Borée *et al.* (1996, 1997) cannot be captured by (2.10), possibly indicating further limitations of the constant-spreading-angle assumption in real transient jets. Nevertheless, the characteristic features of the deceleration transient in Witze's data in figure 4 are well captured by (3.1) and its solution in (3.6).

Borée *et al.* (1996) also derived a partial differential equation for the axial velocity on the centreline during the deceleration transient, somewhat akin to (2.10). They postulated that velocity disturbances would propagate at the fastest velocity in the jet, which is on the centreline. With their formulation, they used the method of characteristics to predict the decay of the axial velocity quite well, though the timing of the arrival of the momentum transient (i.e. the entrainment wave) was somewhat late. They attributed the timing error to a failure to account for pressure effects, which they argued would accelerate the disturbance.

Overall, the solutions of both the hyperbolic equation for centreline velocity of Borée *et al.* (1996) and the first-order wave equation for integral momentum flux employed here agree reasonably well with experimental data. It is interesting to note that wave speed of (2.10) and the centreline velocity of (2.3) as used by Borée *et al.* (1996) have similar magnitudes, though the wave speed derived here is not directly a function of the centreline velocity. The wave speed in (2.10) depends only on the integral momentum flux and not specifically on the local velocity anywhere in the jet, including the centreline. It is therefore unclear if the physical effect governing the speed at which the momentum transient is propagated downstream is the centreline velocity, as argued by Borée *et al.* (1996), or rather the integral momentum flux relative to the integral momentum, as derived here, in (2.10).

3.2. *Entrainment rate*

Some insight into the momentum exchange with ambient fluid that causes the velocity decay during the deceleration transient may be gained by further consideration of the analytical solution in (3.6). In the momentum-transient portion of the jet, using (3.6)

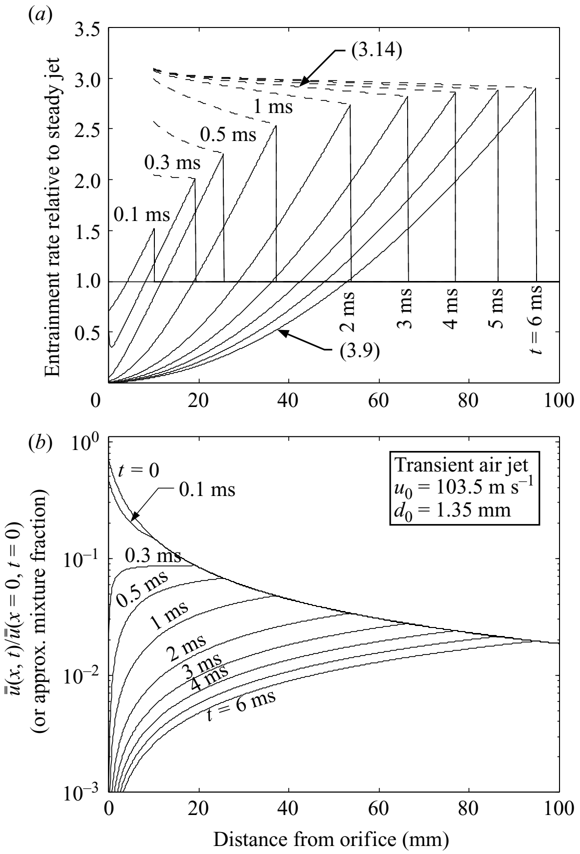

FIGURE 5. (*a*) Entrainment rate relative to steady jet ((3.9), solid lines) or entrainment rate per unit of injected fluid relative to steady jet ((3.14), dashed lines) for the simulated jet of Witze (1980, 1983) at various times after the beginning of the deceleration transient. (*b*) Cross-sectionally averaged jet velocity normalized by the jet exit velocity, which is also the approximate mixture fraction.

for $\sqrt{\dot{M}}$, the entrainment rate from (2.12) is

$$\frac{\partial \dot{m}_e}{\partial x} = \sqrt{\frac{\pi\rho}{\beta}}\tan(\theta/2)\left[\sqrt{\dot{M}} + \frac{(x')^2\tan\left(\dfrac{\theta}{2}\right)\sqrt{\dfrac{\pi\rho\dot{M}_0}{\beta}}\dfrac{1}{8t_{1/2}}}{\sqrt{\dot{M}}+\left(\dfrac{t}{2t_{1/2}}-1\right)\dfrac{\sqrt{\dot{M}_0}}{2}}\right]. \tag{3.8}$$

Dividing (3.8) by (2.13) gives μ, the entrainment rate relative to that of the initial steady jet:

$$\mu = \frac{(\partial \dot{m}_e/\partial x)}{(\partial \dot{m}_{e,Steady}/\partial x)} = \frac{1}{\sqrt{\dot{M}_0}}\left[\sqrt{\dot{M}} + \frac{(x')^2\tan\left(\dfrac{\theta}{2}\right)\sqrt{\dfrac{\pi\rho\dot{M}_0}{\beta}}\dfrac{1}{8t_{1/2}}}{\sqrt{\dot{M}}+\left(\dfrac{t}{2t_{1/2}}-1\right)\dfrac{\sqrt{\dot{M}_0}}{2}}\right]. \tag{3.9}$$

Using solution (3.6), the normalized entrainment rate of (3.9) is plotted as solid lines in figure 5(*a*) at various times after the beginning of the deceleration transient for

Witze's jet. Figure 5(a) shows that during and after the deceleration transient, a wave of increased entrainment (relative to the steady jet) travels downstream. The increased entrainment in the solution is also supported by the experimental data of Borée *et al.* (1996, 1997), which indicate that a region of increase in entrainment propagates downstream during and after the transient deceleration in their air jet.

During the first millisecond of the transient in figure 5(a), the entrainment wave grows in time, with the relative entrainment rate at its leading edge approaching a value of $\mu = 3$. This asymptotic behaviour is consistent with (3.2) in the long-time limit, completely independent of any assumed deceleration transient function (such as (3.5)). To demonstrate the asymptotic behaviour of (3.2), it is first differentiated with respect to x and using (3.3),

$$\frac{\partial\sqrt{\dot{M}}}{\partial x} = \frac{\partial f(\phi)}{\partial\phi}\frac{\partial\phi}{\partial x} = \frac{\partial f(\phi)}{\partial\phi}\left(2x' - 4\cot(\theta/2)\sqrt{\frac{\beta}{\pi\rho}}t\frac{\partial\sqrt{\dot{M}}}{\partial x}\right).$$

Rearranging for $\partial\sqrt{\dot{M}}/\partial x$ and substituting into (3.8) and using (3.3) for $(x')^2$, the entrainment rate is

$$\frac{\partial\dot{m}_e}{\partial x} = \sqrt{\frac{\pi\rho}{\beta}}\tan(\theta/2)\left[\sqrt{\dot{M}} + \frac{2(\partial f(\phi)/\partial\phi)\left(\phi + 4\cot\left(\dfrac{\theta}{2}\right)\sqrt{(\beta/\pi\rho)}\sqrt{\dot{M}}t\right)}{1 + 4(\partial f(\phi)/\partial\phi)\cot(\theta/2)\sqrt{(\beta/\pi\rho)t}}\right]. \tag{3.10}$$

In the transient region, (3.4) and (3.5) show that ϕ is finite, so in the limit of $t \to \infty$, (3.10) becomes

$$\frac{\partial\dot{m}_e}{\partial x}(t \to \infty) = 3\tan(\theta/2)\sqrt{\frac{\pi\rho}{\beta}}\sqrt{\dot{M}}. \tag{3.11}$$

Equation (3.10) shows that early in the deceleration transient, the entrainment rate is dependent on the gradient $\partial f(\phi)/\partial\phi$ of the velocity boundary condition at the nozzle, but in the long-time limit, (3.11) shows that the influence of the boundary condition disappears. Also, since $\sqrt{\dot{M}}$ increases with downstream distance within the transient, (3.11) shows that the entrainment rate must also increase, as demonstrated in figure 5(a). Finally, comparing (3.11) at the leading edge of the entrainment wave, where $\dot{M} = \dot{M}_0$, to the steady-jet entrainment of (2.13), we see that consistent with the asymptotic behaviour illustrated in figure 5(a), the entrainment rate at the leading edge of the entrainment wave in the long-time limit is three times that of the steady jet:

$$\mu_{Edge,t\to\infty} = \frac{(\partial\dot{m}_e/\partial x)\,(\text{edge}, t \to \infty)}{(\partial\dot{m}_e/\partial x)\,(\text{steady jet})} = 3. \tag{3.12}$$

The implications of (3.12) are significant. Equation (3.12) is universal, in that none of the physical characteristics of the jet appears – neither the jet spreading angle nor the boundary conditions affect the limiting behaviour. Therefore, for the simplifying assumptions employed here, the peak entrainment rate at the sharp leading edge of the entrainment wave universally and asymptotically approaches three times that of the initial steady jet in the long-time limit.

The rate at which the entrainment wave reaches the limiting entrainment rate expressed in (3.12) depends on the deceleration rate. With a longer $t_{1/2}$ in (3.6), which implies smaller $\partial f(\phi)/\partial\phi$ in (3.10), the entrainment rate reaches the limiting behaviour more slowly. Witze's jet has a relatively short $t_{1/2}$ (0.15 ms), so the entrainment rate approaches the limiting behaviour quickly, within the measurement region. By

	Air jet	Air jet	Diesel
Experiment	Witze (1980)	Borée *et al.* (1996)	Cossali *et al.* (1996)
Injected ρ (kg m^{-3})	1.2	1.2	820
Ambient ρ (kg m^{-3})	1.2	1.2	5.06
Nozzle diameter (mm)	1.35	5	0.25
Effective diameter (mm)	1.35	5	3.2
Peak velocity (m s^{-1})	103.5	40	$\sim$270
$t_{1/2}$ (ms)	0.15	10	$\sim$0.8
Source figure	–	13	6b
Downstream distance (mm)	92	200	57.5
Time after peak velocity (ms)	3	10	0.25
Measured peak μ (–)	–	$\sim$1.7	$\sim$1.2
Calculated peak μ (–)	2.82	1.67	1.27

TABLE 1. Comparison of measured and analytical peak entrainment rate increase.

contrast, the decelerating jet of Borée *et al.* (1996, 1997) has a slower deceleration, with $t_{1/2}$ near 10 ms. As shown in table 1, using the parameters for their jet in (2.12), including $t_{1/2} = 10$ ms, at a distance of 200 mm downstream (40 diameters), μ reaches a value of 1.67, significantly less than the limiting value of $\mu = 3$. Their measured data are consistent, showing a 70 % increase in entrainment at 40 diameters downstream (Borée *et al.* 1996). In diesel jets, the data of Cossali *et al.* (1996) also show significantly lower peak entrainment rates than (3.9), within their measurement region. As shown in table 1, the deceleration transient in Cossali *et al.* (1996) was relatively slow, so that the peak entrainment rate increased by only 20 % within the downstream range of their measurements. The predictions from (3.9) for such slow injection ramp-down rates show that the relative entrainment rate does not approach the asymptotic value of three within the measurement region. Note that for the diesel jets, to account for the difference in the density of the injected and ambient fluids, the effective (Ricou & Spalding 1961) or momentum (Nathan *et al.* 2006) diameter $d_{eff} = d_0 \cdot \sqrt{\rho_{inj}/\rho_{ambient}}$ was used in (3.9). Modern diesel injectors typically have $t_{1/2} = 0.2$ ms or less, so that the peak entrainment rate can reach $\mu = 2$ or more within the combustion chamber. The data from Cossali *et al.* (1996) also show that the increase in entrainment due to the entrainment wave is imperceptible near the nozzle, but it increases to a measurable level farther downstream, as shown by (3.9). Similar behaviour was observed in a three-dimensional computational study by Iyer & Abraham (2003), who simulated the experiments of Cossali *et al.* (1996). They found that when using a rapid deceleration, the spike in the computed entrainment velocity after the deceleration transient increased with downstream distance. When they used a slower deceleration rate more representative of the experimental conditions, the spike in entrainment became much less pronounced.

To further explore the entrainment wave and to better understand its behaviour, more experimental measurements of the entrainment rate in both single-phase jets and diesel sprays would be helpful. Since the entrainment wave develops more rapidly in jets with more rapid deceleration transients, measurements from such jets would be most valuable. In addition to the rate at which the limiting behaviour of (3.11) is approached, real jets do not show such a sharp peak in the entrainment profile as that shown in figure 5(*a*). Rather, the peak in entrainment is much broader than in figure 5(*a*) for both the air jets of Borée *et al.* (1996, 1997) and the diesel jets of Cossali *et al.* (1996). It is likely that the turbulent axial diffusion processes in real jets, which were excluded in the development of (2.10) (assumption (iii)), act to broaden the sharp leading edge of the entrainment wave. As a result, the transition at the leading edge of the entrainment wave is smoothed, and the peak entrainment rate in real jets should not be so large as shown in figure 5(*a*). Even if real mixing processes reduce the 'peak' entrainment rate at the leading edge of the entrainment wave, however, continuity still demands that as long as the constant spreading angle is maintained, the 'total' increase in entrainment integrated over the transient region must be the same as for the sharp entrainment-wave solution. Thus, in real jets, the total entrainment during the transient is not reduced by axial mixing – it is only redistributed along the jet axis compared to the solution in figure 5(*a*).

The mean velocity $\bar{u}$ in the jet may be determined from the $\sqrt{\dot{M}}$ solution of (3.6), using (2.4) and $\beta = 2$ (fully developed), which is appropriate for all but the near-nozzle region. The mean velocity solution from (3.6), normalized by the jet exit velocity, is plotted in figure 5(*b*). As a result of applying a uniform β throughout the jet, the normalized velocity does not approach unity at the nozzle but rather $\sqrt{1/\beta}$. (Using $\beta = 1$, which is appropriate for the uniform velocity profile at the nozzle, would have produced unity normalized velocity at the nozzle.) Also, a log scale is used in figure 5(*b*) to improve readability for the low velocities that exist in most of the jet.

As the entrainment wave in figure 5(*a*) passes, the velocity in figure 5(*b*) immediately falls below that of the steady jet. As the local velocity is reduced over time because of the increased entrainment of low-momentum ambient fluid, the local velocity gradient (or, equivalently, the $\partial\sqrt{\dot{M}}/\partial x$ gradient) is also reduced. Hence, according to (2.12), the local entrainment rate must decrease as well. As a result, after the entrainment wave passes, the jet fluid becomes increasingly stagnant, so that the local entrainment rate approaches zero. In the long-time limit, therefore, the entrainment wave leaves in its wake a stagnant jet with an absolute entrainment rate approaching zero.

Finally, with knowledge of the peak magnitude of the increased entrainment rate, the earlier assumption that the axial pressure gradient in the decelerating jet is negligible may be examined. The entrained gas velocity $\bar{u}_e$ at the jet boundary is the entrainment rate divided by the product of the density and the jet circumference:

$$\bar{u}_e(\text{edge}, t \to \infty) = \frac{(\partial \dot{m}_e/\partial x)(t \to \infty)}{\rho \cdot (2\pi R)} = \frac{3\tan(\theta/2)\sqrt{(\pi\rho/\beta)}\sqrt{\dot{M}}}{2\rho\pi\tan(\theta/2)x'} = \frac{3\sqrt{(\dot{M}/\pi\rho\beta)}}{2x'}.$$

Using (2.4), the ratio of the entrainment velocity to the jet mean cross-sectionally averaged axial velocity is

$$\frac{\bar{u}_e}{\bar{\bar{u}}} = \frac{\dfrac{3\sqrt{(\dot{M}/\pi\rho\beta)}}{2x'}}{\sqrt{(\dot{M}/\pi\rho\beta)}(\cot(\theta/2)/x')} = \frac{3\tan(\theta/2)}{2}.$$

With $\theta = 28°$, the entrainment velocity in a steady jet is about 37 % of the jet mean cross-sectionally averaged axial velocity (or, using (2.3) in the fully developed jet, about 10 % of the centreline axial velocity). Applying the Bernoulli equation outside of the jet boundary, where viscous effects are negligible, we see that the inertial term of the entrainment flow relative to that of the fully developed jet flow (using $\beta = 2$) is

$$\frac{\frac{1}{2}\rho(\bar{u}_e)^2}{\frac{1}{2}\beta\rho(\bar{\bar{u}})^2} = \frac{9\tan^2(\theta/2)}{4\beta} = 0.07. \tag{3.13}$$

Equation (3.13), along with the equivalence of the inertial terms with pressure (from Bernoulli), show that the static pressure difference between the far field ambient and the jet boundary, as defined here, is about 7 % of the mean stagnation pressure of the axial jet flow. Therefore, if the sharp leading edge of the entrainment wave with three times the steady-jet entrainment rate is maintained, the pressure drop relative to the ambient becomes significant (7 %) and could have a significant affect on the solution. But, as described above, finite injection ramp-down rates and axial mixing in real jets reduce and broaden the leading edge of the entrainment wave, so that the peak entrainment rate may only be twice that of a steady jet, or even less. With a factor of two or less local increase in entrainment, the pressure difference is only 3 % or less of the mean stagnation pressure of the jet flow. (Incidentally, in a steady jet, the constant pressure assumption is well justified, since (3.15) for the steady jet shows that the pressure difference from ambient is less than 1 % of the mean stagnation pressure of the jet flow and that the axial gradient in pressure is very small.)

3.3. *Scalar mixing*

In addition to the effects of the deceleration transient and entrainment wave on jet momentum, the effects on scalar mixing may be estimated from the axial-velocity solution. To illustrate the general behaviour of scalar mixing, a simplifying assumption of unity Schmidt number may be applied. Then, the jet fluid is transported equally with velocity, so that the local mixture fraction can be represented by the local axial velocity relative to the original nozzle exit velocity. That is, for unity Schmidt number, the normalized cross-sectionally averaged velocity $\bar{\bar{u}}/u_0$ in figure 5(*b*) also represents the cross-sectionally averaged mixture fraction $\bar{\bar{Z}}$. An additional assumption in using $\bar{\bar{Z}} \approx \bar{\bar{u}}/u_0$ is that all of the jet fluid initially carried the same momentum. This assumption is true for all of the fluid in the initial steady jet but not for fluid injected during the deceleration transient. Assuming that the amount of fluid in the rapidly ending transient is relatively small, however, the equivalence of mixture fraction with the normalized axial velocity is justified for nearly all of the downstream jet. Only in the near-nozzle region is the mixture fraction not well represented by the normalized axial velocity.

Interpreting the normalized velocity plots in figure 5(*b*) as mixture fraction, during and after the deceleration transient, the mixtures in the jet are rapidly diluted with the ambient fluid as the entrainment wave propagates downstream. Indeed, less than 1 ms into the deceleration transient, the axial mixture fraction gradient transitions from negative to a positive. That is, within the wake of the entrainment wave, the upstream mixture fraction becomes lower than downstream, which is opposite to mixtures in a steady jet. This trend agrees well with fuel concentration measurements in decelerating single-phase jets (Borée *et al.* 1997; Johari & Paduano 1997) and two-phase diesel jets (Kim & Ghandhi 2001; Bruneaux 2005; Musculus *et al.* 2007; Genzale *et al.* 2008). Incidentally, as described in the introduction, the opposite behaviour is observed in 'accelerating' jets, where the momentum flux $\partial\dot{M}/\partial t$ at the nozzle is positive, so the momentum flux gradient $\partial\dot{M}/\partial x$ is negative. According to (2.12), the entrainment rate is then lower relative to a steady jet, so that the mixture fraction increases, as is observed experimentally (Kato *et al.* 1987; Zhang & Johari 1996).

In addition to analysing the behaviour of the absolute entrainment rate, it is also interesting to study the rate of entrainment per unit of injected fluid (e.g. fuel). The mixing per unit of injected fluid ($\partial\dot{m}_e/\partial m_f$) can be expressed as the ratio of the entrainment rate ($\partial\dot{m}_e/\partial x$) to the local axial gradient of injected fluid in the jet ($\partial m_f/\partial x$). As shown in (2.12), the entrainment rate $\partial\dot{m}_e/\partial x$, or entrainment per unit distance, is the axial gradient of mass flux. In a parallel fashion, the local mass of fluid in the jet per unit distance $\partial m/\partial x$ can be represented by the axial gradient of the mass of jet fluid:

$$\frac{\partial m}{\partial x} = \frac{\partial}{\partial x}(\rho V) = \rho A.$$

The local mass per unit distance of 'injected' fluid is then the product of $\partial m/\partial x$ and the local cross-sectionally averaged mixture fraction $\bar{\bar{Z}}$. As described above, $\bar{\bar{Z}}$ may be approximated by the normalized velocity $\bar{\bar{u}}/u_0$, and since the local area is the same for the steady jet and the transient jet (assumption number five), the entrainment rate per unit of injected jet fluid in the transient jet relative to that of the steady jet (μ_Z) is

$$\mu_Z = \frac{(\partial \dot{m}_e/\partial x)/\rho A\bar{\bar{Z}}}{(\partial \dot{m}_{e,Steady}/\partial x)/\rho A\bar{\bar{Z}}_{Steady}} = \frac{\bar{\bar{u}}_{Steady}/u_0}{\bar{\bar{u}}/u_0}\mu = \frac{\sqrt{\dot{M}_0}}{\sqrt{\dot{M}}}\mu. \tag{3.14}$$

In figure 5(a), the μ_Z solution at several times after the start of injection is plotted as the dashed lines. The solutions are not plotted upstream of 10 mm from the nozzle exit because of the inaccuracies of equating relative velocity with mixture fraction in the near-nozzle region in which the initial momentum carried by the injected fluid is not constant, as described earlier. After normalizing by the local mixture fraction relative to that of the steady jet, figure 5(a) shows that the relative entrainment rate per unit of injected fluid in the wake of the entrainment wave is nearly constant axially.

The above solution is also consistent with the entrainment rate of (3.10) in the long-time limit, even away from the leading edge of the entrainment wave. Using (3.14) with (3.10) as $t \to \infty$,

$$\mu_Z = 3. \tag{3.15}$$

Thus, even though the relative entrainment rate of (3.9) decreases after the passage of the entrainment wave, the relative entrainment rate 'per unit of injected fluid' of (3.15) asymptotes to a factor of three higher than in the initial steady jet. Furthermore, figure 5(b) shows that the μ_Z value is reached throughout the entire wake of the entrainment wave, even in regions in which μ is less than in a steady jet. The μ_Z value is relatively constant in the wake of the entrainment wave because regions with a lower entrainment rate have proportionally lower concentrations of injected fluid, so that the normalized entrainment rate is unchanged. The factor-of-three increase in the mixing rate behind the entrainment wave is also consistent with molecular mixing measurements by Johari & Paduano (1997) for a gravity-driven water jet. Based on a reduced reaction length for their single-pulsed jet compared to a steady jet, they concluded that the mixing rate was increased by more than a factor of two after the deceleration phase.

The reader is cautioned that the above conclusions about the increase in entrainment after the passage of the entrainment wave must be interpreted carefully. Equations (3.9) and (3.12) do not imply that the total entrainment rate integrated over the whole jet increases by a factor of three compared to a steady jet. Figure 5(a) shows that entrainment is greater than a steady jet near the front of the entrainment wave, but entrainment is much less behind it. Visual inspection (and numerical integration) of figure 5(a) shows that the total entrainment rate, which is the area under any of the relative entrainment curves, is not much greater than for a steady jet (area under horizontal line at relative entrainment rate of unity). The entrainment wave redistributes the entrainment to where it is 'needed', so that more entrainment occurs in regions that have higher concentrations of injected fluid, and less entrainment occurs in regions with lower concentrations of injected fluid. As a result, the local entrainment rate per unit of injected fluid eventually approaches three times that of a steady jet, throughout the wake of the entrainment wave, as shown by (3.15).

The implications of the above observations for mixing after the end of fuel injection in diesel engines are profound. It is well recognized that if combustion can be delayed until after the end of fuel injection, the fuel has more time to premix with the in-cylinder air before combustion, so that local fuel concentrations and subsequent soot formation can be reduced. However, (3.15) shows that it is not simply the extended ‘time’ for premixing that is important, but rather the increase in the mixing ‘rate’ by up to a factor of three throughout the jet because of the passage of the entrainment wave that promotes premixing before combustion. If the rate of entrainment per unit injected fluid after the end of injection were to remain the same as in the quasi-steady jet, then the time required to achieve a desired level of premixing would be up to three times greater. Such a relatively slow mixing rate would profoundly limit the potential of modern diesel operational strategies to prepare mixtures necessary to achieve low pollutant emissions in the time available before combustion. The threefold increase in mixing following the end of injection must certainly play a role in soot oxidation and late-cycle combustion processes as well. The ultimate soot emitted from the engine is almost certainly reduced by increased oxidation due to the mixing enhancements of the entrainment wave. Recognition of the considerable increase in the mixing rate caused by the entrainment wave offers the possibility that fuel delivery strategies for diesel engines could be designed and optimized to take advantage of it.

Also, the earlier conclusion that the rate of approach to the limiting entrainment rate of $\mu = 3$ is controlled by deceleration rate also indicates that the rate at which the $\mu_Z = 3$ asymptote is approached is affected by the injection rate shape in diesel engines. This suggests that the injection rate shape may be tailored to deliver a desired mixture distribution at a given time after the end of injection. Previous studies have shown that for accelerating jets, the acceleration rate may be adjusted to decrease mixing (Kato *et al.* 1987). Here, for decelerating jets, the deceleration rate may be adjusted to increase mixing. If more mixing is desired, a faster deceleration rate should be used. On the other hand, if less mixing is desired after the ending transient, such as when mixtures can become too lean for complete combustion in diesel engines, (Musculus *et al.* 2007), the deceleration rate could be decreased. More details of the effects of the deceleration rate on mixing in diesel jets from a numerical solution of a discretized wave equation may be found in Musculus & Kattke (2009).

Finally, the action of the entrainment wave is also likely to play a role in modulated jets and flames, for which the nozzle exit velocity fluctuates over time. Modulated jets typically have greater mean entrainment, and often greater spreading angles, than steady jets (Bremhorst 1979), and modulated flames typically have shorter flame lengths, indicating faster mixing (Lakshminarasimhan, Clemens & Ezekoye 2006). The entrainment wave should be important especially in fully modulated jets, which reach zero velocity at the nozzle between pulses and can have entrainment rates that are several times greater than a steady jet (Bremhorst 1979; Bremhorst & Hollis 1990). Also, the near-nozzle increase in momentum observed in fully pulsed jets (Bremhorst & Hollis 1990) may be related to the action of the entrainment wave or its effect on pressure (see (3.13)). The entrainment wave should be important even for partially modulated jets and flames because (2.10) shows that a decrease in the exit velocity of any magnitude will propagate downstream as an entrainment wave.

3.4. *Post entrainment-wave penetration*

One final issue worthy of investigation is the change in penetration rate caused by the entrainment wave. As described earlier, the wave speed given by (2.10) is twice the jet penetration rate. This means that the entrainment wave reaches the head of a single jet pulse at a time of approximately two pulse durations. When the entrainment wave reaches the head of the jet, the increased entrainment of low-axial-momentum ambient fluid reduces the velocity at the head from what it would be for a steady jet.

Consequently, the penetration function must decrease from the $t^{1/2}$ dependence of (2.15) to some slower rate. No analytical solution for the penetration rate after the arrival of the entrainment wave is apparent, but it may be determined by numerical integration.

Inserting the $\sqrt{\dot{M}}$ solution of (3.6) into (2.14), the penetration rate of the head after the arrival of the entrainment wave is

$$c_{Head} = \sqrt{\frac{\beta}{\pi\rho}}\,\frac{\cot(\theta/2)}{x'}\left[\begin{array}{l}\sqrt{\left(\dfrac{t}{2t_{1/2}}-1\right)^2\dfrac{\dot{M}_0}{4}-\tan\left(\dfrac{\theta}{2}\right)\sqrt{\dfrac{\pi\rho\dot{M}_0}{\beta}}\,\dfrac{(x_0)^2-(x')^2}{8t_{1/2}}}\\ -\left(\dfrac{t}{2t_{1/2}}-1\right)\dfrac{\sqrt{\dot{M}_0}}{2}\end{array}\right]. \tag{3.16}$$

Using (2.15) for the penetration of the head of the jet until a time equal to two injection durations and thereafter numerically integrating (3.16), the jet penetration before and after the arrival of the entrainment wave at the head may be calculated.

For comparison with experimental data, penetration measurements of pulsed water jets by Sangras *et al.* (2002) are offered. Most of the jets they studied had very short injections that produced puffs of fluid dominated by the head vortex dynamics rather than by quasi-steady-jet processes following in a temporarily sustained jet. Some of their ‘intermittent’ jets with longer injection durations, however, had short quasi-steady periods and are therefore marginally suitable for comparison. In particular, their water jet with a nozzle diameter of 3.2 mm, a peak injection velocity of 1.85 m s^{-1} and an injection duration of 0.5 s is most appropriate. This jet has the largest injected volume with the shortest starting and ending transients relative to the total injection period, so that it has the longest well-developed quasi-steady-jet period of all those that they studied. Even so, because of a slow starting transient as the injection pump is started, the measured penetration data (symbols) in figure 6 show that the penetration does not follow the $t^{1/2}$ dependence of (2.15) until $t = 0.4$ s, which is near the end of injection. Then, at $t = 1$ s, which is approximately two pulse durations after the start of the pulse, the penetration function changes to a roughly $t^{1/4}$ dependence (Sangras *et al.* 2002). Sangras *et al.* (2002) derived a $t^{1/4}$ penetration relation for puffs by considering the growth of an isolated vortex ball containing the conserved momentum of the puff. The penetration rate in (3.16), which was derived from the solution to the nonlinear wave equation of (3.1) and does not consider any vortex ball dynamics, also captures the transition to $t^{1/4}$ dependence. Solutions of (2.15) (prior to $t = 1$ s) and the numerical integration of (3.16) (after $t = 1$ s) are plotted in figure 6 as the solid line. The penetration solution exceeds the experimental measurements because it does not account for the slow start-up of the pump in the experiment. The penetration solution parallels the experimental data, however, so that the timing of the transition, along with the $t^{1/2}$ and $t^{1/4}$ slopes for the two phases of penetration, is clearly apparent and well captured by (2.15) and (3.16).

The solution of (3.16), as well as insight into of the experimental data of Sangras *et al.* (2002) based on the entrainment-wave concept presented here, shows that jet penetration can be affected in a predictable way according to the timing of the deceleration transient – the penetration rate will decrease markedly after two pulse durations. This observation is important for diesel engines because jet over-penetration

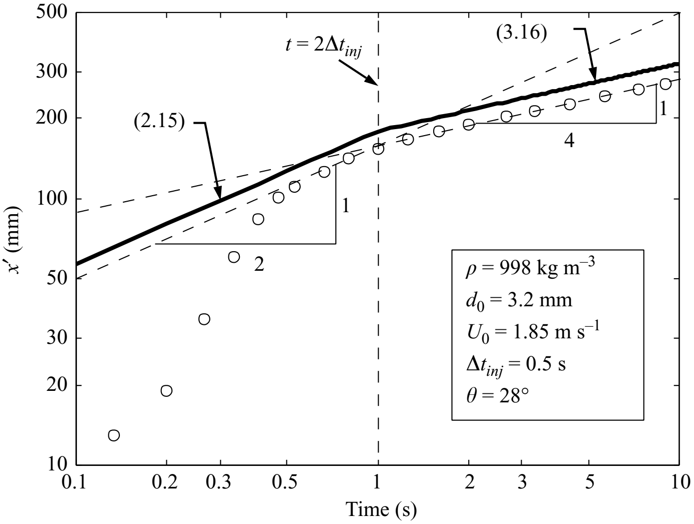

FIGURE 6. Penetration data (circles) and solutions from (2.15) and (3.16) (solid lines) for an intermittent water jet of Sangras *et al.* (2002), as described in the inset.

can be problematic. When the fuel is injected early in the compression stroke, the penetration rate increases because the ambient gases have low density. Furthermore, the in-cylinder temperatures are also low, so the fuel vaporization rate is reduced. As a result, the jet penetrates faster and evaporates later, so that liquid fuel may impinge on and interact with the walls of the combustion chamber, which is generally undesirable because of emissions problems (Kashdan, Mendez & Bruneaux 2007) or lubrication oil dilution (Akagawa *et al.* 1999). To mitigate these liquid–wall interaction problems, the jet penetration may be reduced if the entrainment wave is properly timed to reach the head of the jet before it reaches the in-cylinder surfaces. In addition to slowing the penetration rate, the increase in mixing from the entrainment wave promotes faster fuel vaporization, so that the fuel may be entirely in the vapour phase by the time the jet impinges on in-cylinder surfaces. Both of these effects are most likely already in effect for diesel engines. Even so, with recognition of the importance and magnitude of these mechanisms, diesel fuel-injection strategies may be better designed and optimized to take advantage of the increased mixing caused by the entrainment wave.

4. Summary

A simplified one-dimensional analysis was applied to the decelerating phase of a transient incompressible jet. Based on observations from experiments in the literature, six simplifying assumptions were applied in the analysis: (i) density is constant; (ii) viscous forces outside the control volume are neglected; (iii) axial diffusive mixing is neglected; (iv) the axial pressure gradient is negligible; (v) the jet cross-sectional area remains constant throughout the deceleration transient; and (vi) the radial profiles of axial velocity remain constant during the transient. Using these simplifying assumptions, a transport equation for the integral momentum flux was derived, which had the form of a first-order nonlinear wave equation. Using the method of characteristics, an algebraic analytical solution was offered for a generic initial condition function. Key conclusions from analysis of the solution and its governing transport equation are as follows:

(i) The solution shows that during and after the deceleration transient, a wave of increased entrainment travels downstream at twice the jet penetration rate. As a result, the increased entrainment associated with the jet deceleration not only affects the tail end of the jet in the vicinity of the deceleration but rather eventually affects the entire jet as it propagates downstream. The timing of the arrival of this entrainment wave at the jet head, as well as the velocity decay rate in its wake, agrees well with experimental data.

(ii) The peak entrainment rate at the leading edge of the entrainment wave increases with downstream distance. In the long-time limit, the peak entrainment rate approaches an asymptotic limit that is three times the rate of the initial steady jet.

(iii) The rate at which the asymptotic entrainment rate is approached depends on the speed of the deceleration transient. Slow transients may not approach the asymptotic value within the region of interest. This implies that the deceleration rate may be tailored to produce a desired mixing distribution at a given time after the deceleration transient.

(iv) In the wake of the entrainment wave, the absolute entrainment rate decays to a level below that of the steady jet. However, the entrainment rate relative to the local concentration of injected fluid, which is effectively the mixing rate, remains relatively constant throughout the wake of the entrainment wave, at a level up to three times higher than in the initial steady jet.

(v) After the arrival of the entrainment wave at the head of the jet, the penetration rate transitions from a square-root dependence on time, which is typical of a steady jet, to a fourth-root dependence on time. A similar transition is also observed in experiments.

This work was performed at the Combustion Research Facility, Sandia National Laboratories, Livermore, CA. Sandia is a multi-programme laboratory operated by Sandia Corporation, a Lockheed Martin Company, for the National Nuclear Security Administration of the US Department of Energy (DOE) under contract DEAC04-94AL85000. Financial support was provided by DOE's Office of Vehicle Technologies, programme manager Gurpreet Singh. The author expresses his gratitude to Andy Lutz of Sandia National Laboratories and John Abraham of Purdue University, whose critical discussions helped greatly to shape this effort, and to O. C. Kwon, for graciously providing access to the raw data used in figure 6.

Appendix. Decelerated air-jet analysis

The decelerated air-jet data of Atassi *et al.* (1993) and Borée *et al.* (1996, 1997) is suitable to test the form of the governing nonlinear wave equation in (2.10) by examining the local temporal and spatial gradients of velocity in the middle of the transition. Among their measurements, Borée *et al.* (1996, 1997) reported temporal data of mean axial velocity $\bar{u}_c(x,t)$ on the jet centreline, normalized by the centreline axial velocity $\bar{u}_c(x,t=0)$ of the initial steady jet, at several downstream locations, plotted versus the ratio of the downstream distance x to the nozzle diameter D_0, as shown in figure 7. Their air jet issued from a nozzle of diameter $D_0 = 5\,\mathrm{mm}$ at an initial velocity of $U_{0,1} = 40\,\mathrm{m\,s^{-1}}$. The velocity at the nozzle exit ($x/D_0 = 0$) then decelerates to a lower velocity of $U_{0,2} = 20\,\mathrm{m\,s^{-1}}$ over a period of about 10 ms, starting at $t = 55\,\mathrm{ms}$. Farther downstream in the jet, the departure from the steady velocity occurs later, as the entrainment wave travels downstream. To analyse the local speed of the transient using the velocity data in figure 7, (2.10) must be rewritten in terms

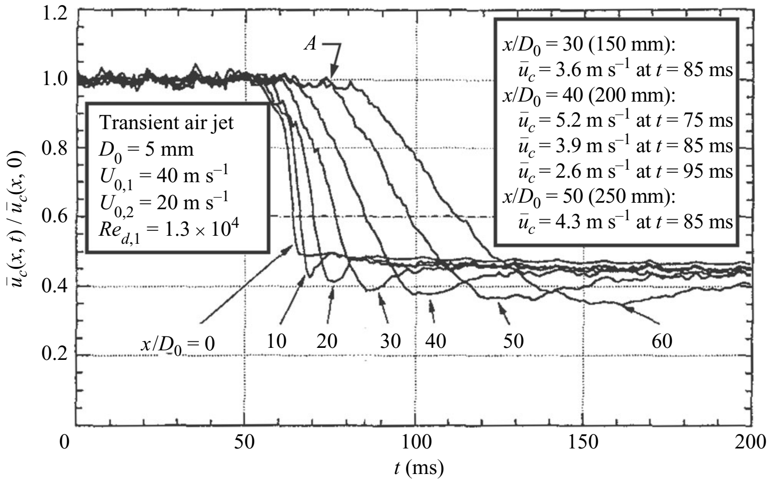

FIGURE 7. Measured ensemble-averaged centreline hot-wire velocity data in an $Re_d = 1.3 \times 104$ air jet issuing from a 5-mm diameter nozzle subject to deceleration from 40 to $20\,\mathrm{m\,s^{-1}}$ at the nozzle exit, normalized by the initial steady-jet centreline velocities (With kind permission from J. Boree and Springer Science + Business Media: Borée *et al.* 1996 (figure 4), © Springer-Verlag 1996).

of the centreline velocity using (2.3) and (2.4):

$$\frac{\partial(\beta\rho A\bar{\bar{u}}^2)}{\partial t} = -c_{wave}\frac{\partial(\beta\rho A\bar{\bar{u}}^2)}{\partial x}. \tag{A 1}$$

In (A1), c_{wave} is the wave speed. Using (2.3) and noting that $\partial A/\partial x = 2A/x$, (A1) may be simplified and rearranged for c_{wave} in terms of $\bar{u}_c$:

$$c_{wave} = \frac{-(\partial\,(\bar{u}_c)/\partial t)}{(\bar{u}_c/x') + (\partial\bar{u}_c/\partial x)}. \tag{A 2}$$

Using (A2), the wave speed may be evaluated anywhere in the transient, rather than only at its leading edge as in the previous analysis. For example at $x/D_0 = 40$ and $t = 85\,\mathrm{ms}$, where the centreline velocity in the transient is 60 % of that for the initial steady jet, the gradients in (A2) may be evaluated using central differences with the absolute velocities listed in the inset in figure 7:

$$\frac{\partial\,(\bar{u}_c)}{\partial t} = \frac{(2.6 - 5.2)\,\mathrm{m\,s^{-1}}}{(95 - 75)\,\mathrm{m\,s}} = -130\,\mathrm{m\,s^{-2}},$$

$$\frac{\partial\,(\bar{u}_c)}{\partial x'} = \frac{4.3 - 3.6}{(50 - 30)\,D_0} = 7\ \mathrm{s^{-1}}.$$

With $\bar{u}_c = 3.9\,\mathrm{m\ s^{-1}}$, (2.10) predicts that the propagation velocity of the transient is

$$c_{wave} = \frac{130\,\mathrm{m\ s^{-2}}}{(3.9\,\mathrm{m\ s^{-1}}/37.5\,\mathrm{mm}) + 7.8\,\mathrm{s^{-1}}} = 4.6\,\mathrm{m\ s^{-1}}.$$

Inspection of figure 7 shows that the 60 % position of the transient travels from $x/D_0 = 30$ at $t = 75\,\mathrm{ms}$ to $x/D_0 = 50$ at $t = 97\,\mathrm{ms}$. The average speed is then $4.5\,\mathrm{m\,s^{-1}}$, which is only slightly less than the $4.6\,\mathrm{m\,s^{-1}}$ speed of (2.10) near $x/D_0 = 40$. For a $1/x$ dependence of axial velocity, however, the average velocity over a spatial interval from $x/D_0 = 30$ to $x/D_0 = 50$ should be approximately 33 % greater than the instantaneous velocity at the midpoint of the interval. The discrepancy is most likely due to real jet processes not captured by (2.10) and because of the constant-spreading-angle and constant-β approximations that were applied during the transient. As described earlier, Atassi *et al.* (1993) showed that in the middle of the transition, the velocity profile becomes flatter and slightly wider, so that β decreases, while A increases by up to 30 % (15 % increase in jet width), which causes the local $\partial A/\partial x$ to decrease. The constant-spreading-angle and constant-β approximations fail to account for these changes, so that (2.10) is somewhat inaccurate 'within' the transient. Analysis of the propagation time of the transient (not shown here), however, show that (2.10) appears to be reasonably accurate at the 'leading edge' of the transient, where the similar velocity profile (constant-β) and constant-spreading-angle assumptions are more likely to be reasonable. Nevertheless, both the propagation time and the propagation speed analyses of experimental data show that the speed of the momentum transient of (2.10) is reasonable and that the transient travels downstream at roughly twice the speed of the initial penetrating jet.

Careful inspection of the decelerated jet data in figure 7 reveals one other important limitation of the assumption of a constant spreading angle during the deceleration transient. For each of the downstream measurement locations in the jet, the centreline velocity falls to minimum that is as much as 30 % below that of the slower jet that follows the initial steady jet. Note that this does not appear to be an artefact of an undershoot in the injection velocity at the nozzle, since no undershoot was measured at $x/D_0 = 0$. Without a velocity undershoot in the initial condition, (3.1) is unable to reproduce a velocity undershoot in the solution. The method of characteristics solution in (3.6) effectively shifts the boundary condition function downstream with time, in a nonlinear fashion. If the boundary condition function had no velocity undershoot, it is therefore impossible for any method of characteristics solution of (3.6) to reproduce the velocity undershoot observed in figure 7. Some real physical effect not included in the analysis, such as the slight increase in the jet width, is likely to be responsible for the velocity undershoot.

REFERENCES

Abramovich, G. N. 1963 Chapter 5. Jet of an incompressible fluid in a coflowing external stream. In *The Theory of Turbulent Jets*. MIT Press.

Akagawa, H., Miyamoto, T., Harada, A., Sasaki, S., Shimazaki, N., Hashizume, T. & Tsujimura, K. 1999 Approaches to solve problems of the premixed lean diesel combustion. *SAE Trans.* **108**(3), 120–132.

Atassi, N., Boree, J. & Charnay, G. 1993 Transient behaivor of an axisymmetric turbulent jet. *Appl. Sci. Res.* **51**, 137–142.

Borée, J., Atassi, N. & Charnay, G. 1996 Phase averaged velocity field in an axisymmetric jet subject to a sudden velocity decrease. *Exp. Fluids* **21**, 447–456.

Borée, J., Atassi, N., Charnay, G. & Taubert, L. 1997 Measurements and image analysis of the turbulent field in an axisymmetric jet subject to a sudden velocity decrease. *Exp. Thermal Fluid Sci.* **14**, 45–51.

Breidenthal, R. 1986 The turbulent exponential jet. *Phys. Fluids* **29**, 2346–2347.

Breidenthal, R. E. 2008 The effect of acceleration on turbulent entrainment. *Phys. Scripta* **T132**, 1–5.

Bremhorst, K. 1979 Unsteady subsonic turbulent jets. In *Recent Developments in Theoretical and Experimental Fluid Mechanics: Compressible and Incompressible Flows* (ed. U. Müller, K. G. Roesner & B. Schmidt) Springer, pp. 480–520.

Bremhorst, K. & Hollis, P. G. 1990 Velocity field of an axisymmetric pulsed, subsonic air jet. *AIAA J.* **28**, 2043–2049.

Bruneaux, G. 2005 Mixing process in high pressure diesel jets by normalized laser induced exciplex fluorescence. Part I. Free jet. *SAE Trans.* **114**(3), 1444–1461.

Cossali, G. E., Geria, A., Coghe, A. & Brunello, G. 1996 Effect of gas density and temperature on air entrainment in a transient diesel spray. *SAE Trans.* **105**(3), 1293–1301.

Crow, S. C. & Champagne, F. H. 1971 Orderly structure in jet turbulence. *J. Fluid Mech.* **48**, 547–591.

Doudou, A. 2005 Turbulent flow study of an isothermal diesel spray injected by a common rail system. *Fuel* **84**, 287–298.

Genzale, C. L., Reitz, R. D. & Musculus, M. P. B. 2008 Effects of piston bowl geometry on mixture development and late-injection low-temperature combustion in a heavy-duty diesel engine. *SAE International Journal of Engines* **1**(1), 913–937.

Hill, P. G. & Ouellette, P. 1999 Transient turbulent gaseous fuel jets for diesel engines. *J. Fluids Engng* **121**, 93–101.

Hinze, J. O. 1975 Chapter 6. Free turbulent shear flows, In *Turbulence*, 2nd ed. McGraw-Hill.

Iyer, V. & Abraham, J. 2003 An evaluation of a two-fluid Eulerian-liquid Eulerian-gas model for diesel sprays. *J. Fluids Engng* **125**, 660–669.

Johari, H. & Paduano, R. 1997 Dilution and mixing in an unsteady jet. *Exp. Fluids* **23**, 272–280.

Joshi, A. & Schreiber, W. 2006 An experimental examination of an impulsively started incompressible turbulent jet. *Exp. Fluids* **40**, 156–160.

Kashdan, J. T., Mendez, S. & Bruneaux, G. 2007 On the origin of unburned hydrocarbon emissions in a wall-guided, low NO_2 diesel combustion system. *SAE Trans.* **116**(4), 234–257.

Kato, S. M., Groenewegen, B. C. & Breidenthal, R. E. 1987 Turbulent mixing in nonsteady jets. *AIAA J.* **25**, 165–168.

Kevorkian, J. 1996 *Partial Differential Equations.* Chapman & Hall.

Kim, T. & Ghandhi, J. B. 2001 Quantitative two-dimensional fuel vapour concentration measurements in an evaporating diesel spray using the exciplex fluorescence method. *SAE Trans.* **110**(3), 2165–2181.

Lakshminarasimhan, K., Clemens, N. T. & Ezekoye, O. A. 2006 Characteristics of strongly-forced turbulent jets and non-premixed jet flames. *Exp. Fluids* **41**, 523–542.

Levandosky, J. 2008 Stanford MA220 lecture notes. http://www.stanford.edu/class/math220a/handouts/firstorder.pdf.

Musculus, M. P. B. & Kattke, K. 2009 Entrainment waves in diesel jets. to appear in SAE International Journal of Engines 2.

Musculus, M. P. B., Lachaux, T., Pickett, L. M. & Idicheria, C. A. 2007 End-of-injection over-mixing and unburned hydrocarbon emissions in low-temperature-combustion diesel engines. *SAE Trans.* **116**(3), 515–541.

Naber, J. D. & Siebers, D. L. 1996 Effects of gas density and vaporization on penetration and dispersion of diesel sprays. *SAE Trans.* **105**(3), 82–111.

Nathan, G. J., Mi, J., Alwahabi, Z. T., Newbold, G. J. R. & Nobes, D. S. 2006 Impacts of a jet's exit flow pattern on mixing and combustion performance. *Prog. Energy Combust. Sci.* **32**, 496–538.

Pickett, L. M. 2009 Engine combustion network. http://public.ca.sandia.gov/ecn/.

Reynolds, W. C., Parekh, D. E., Juvet, P. J. D. & Lee, M. J. D. 2003 Bifurcating and blooming jets. *Annu. Rev. Fluid Mech.* **35**, 295–315.

Ricou, F. P. & Spalding, D. B. 1961 Measurements of entrainment by axisymmetrical turbulent jets. *J. Fluid Mech.* **11**, 21–32.

Sangras, R., Kwon, O. C. & Faeth, G. M. 2002 Self-preserving properties of unsteady round nonbuoyant turbulent starting jets and puffs in still fluids. *ASME J. Heat Trans.* **124**, 460–469.

Schlichting, H. 1979 Chapter XXIV. Free turbulent flows: jets and wakes. In *Boundary Layer Theory*, 7th ed. McGraw-Hill.

Witze, P. O. 1980 The impulsively started incompressible turbulent jet. *Energy Rep.* SAND80-8617. Sandia National Laboratories.

Witze, P. O. 1983 Hot-film anemometer measurements in a starting turbulent jet. *AIAA J.* **21**, 308–309.

Wu, K.-J., Santavicca, D. A. & Bracco, F. V. 1984 LDV measurements of drop velocity in diesel-type sprays. *AIAA J.* **22**, 1263–1270.

Zhang, Q. & Johari, H. 1996 Effects of acceleration on turbulent jets. *Phys. Fluids* **8**, 2185–2195.